Thiophene-backbone Arcuate Graphene Nanoribbons: Shotgun Synthesis and Length-dependent Properties

Ruiying Zhang,[1] Xinyu Chen,[1] Lingyun Zhu,[1] Yanxia Huang,[1] Zi'ang Zhai,[1] Qiang Wang,[1] Lingding Wang,[1] Taosong Wang,[1] Wei-Zhen Wang,[1] Ke-Yin Ye,[1]* and Yuanming Li[1,2]*

[1]Key Laboratory of Molecule Synthesis and Function Discovery, Fujian Province University, College of Chemistry at Fuzhou University, Fuzhou, Fujian, 350108, China

[2]State Key Laboratory of Elemento-Organic Chemistry, Nankai University, Tianjin, 300071, China

ABSTRACT: Efficient synthetic methods are urgently needed to produce graphene nanoribbons (GNRs) with diverse structures and functions. Precise control over the topological edges of GNRs is also crucial for achieving diverse molecular topologies and desirable electro-optical properties. This study demonstrates a highly efficient "Shotgun" synthesis of thiophene-backbone arcuate GNRs, offering a significant advantage over tedious iterative synthesis. This method utilizes a one-pot, three-component Suzuki-Miyaura coupling for the precursor, followed by a Scholl reaction for cyclization. The resulting arcuate GNRs have sulfur atoms embedded in the carbon backbone with a combined armchair, cove, and fjord edge structure. This multi-edge architecture is further modified by high-yield oxidation of the electron-rich sulfur atoms to electron-deficient sulfones, enabling precise regulation of the GNRs' electronic properties. This arcuate GNRs with diverse edge structures, heteroatom doping and precise lengths, opening exciting avenues for their application in optoelectronic devices.

Introduction

Atomically precise graphene nanoribbons (GNRs) have attracted significant attention recently due to their intriguing electronic properties and applications in next-generation optoelectronic devices.[1] Their optical and electronic properties strongly depend on their structures, such as lengths, widths, shapes, and edges.[2] Besides control over the above-mentioned structural parameters, properties can be fine-tuned by incorporation of heteroatoms into the conjugated nanoribbon backbones.[3] Organic chemists have focused on developing new synthetic strategies and easily accessible structure-rich building blocks for the production of GNRs as well as heteroatom-doped GNRs over decades.[4]

The solution-phase synthesis, that is the formation of a linearly extended precursor followed by a ring-closing step is one of the most promising strategies for the preparation of well-defined GNRs on a large scale.[5] To the study of length-dependent photophysical properties via comparison with their linear counterparts, GNRs with different lengths are usually prepared by iterative synthesis (Figure 1a).[2d, 3d, 6] These methods often involve complex and expensive starting materials, restricting structural and functional diversity. Inspired by the "shotgun" approach to macrocycle,[7,8] which involves using a one-pot multicomponent cyclization of small monomers, to access the macrocycle. This approach shows great advantages to quick constructing different size macrocycle. In addition, phenanthrene as an important polycyclic aromatic hydrocarbon (PAH), which with armchair side. We envision that 1,8-diaryl phenanthrene derivative would be promising building blocks for GNRs, which are readily available.[9] Herein, we report a series of arcuate GNRs with thiophene-backbones, achieved by "Shotgun" approach with high efficiency. The precursor of GNRs was constructed by the Suzuki-Miyaura coupling with 1,8-diaryl phenanthrene as key building block and then dehydrocyclization to obtain GNRs of different lengths. In this case, three GNRs (**AR-11**, **AR-17**, and **AR-23**) with multiple edge structures were achieved (the numbering indicates the number of longitudinally fused rings along their backbone) (Figure 1a). Oxidizing electron-rich sulfur atoms to electron-deficient sulfones yielded **ARO-11** and **ARO-17** with high efficiency, respectively. Detailed theoretical and experimental studies demonstrate that length and oxidation state greatly affects not only molecular conformations but also electronic structures and photophysical properties.

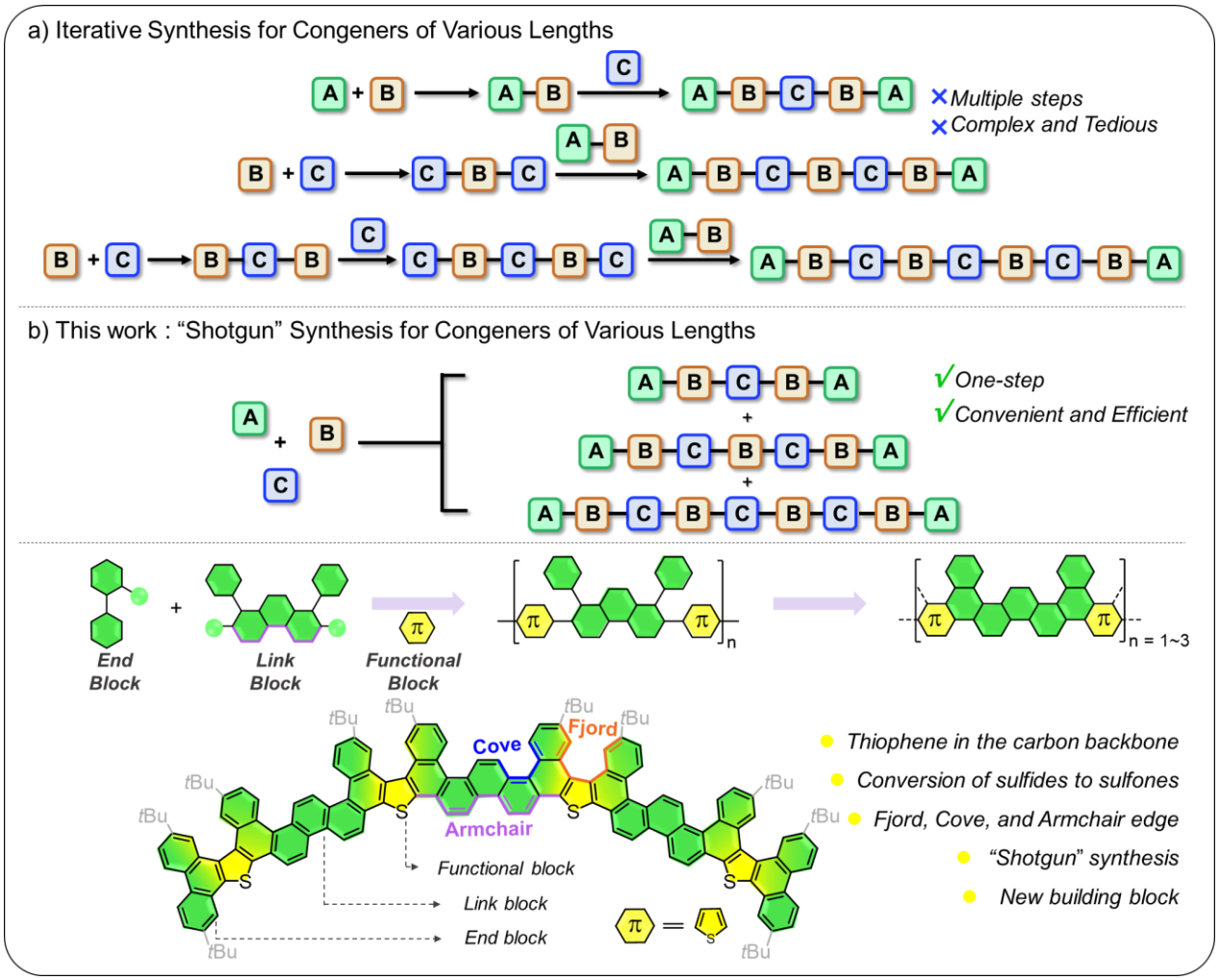

Figure 1. a) The precursor of GNRs was constructed by iterative strategy. b) Schematic illustration of construction of thiophene-backbone arcuate GNRs via "Shotgun" approach.

Results and Discussion

Synthesis

To achieve a concise "Shotgun" synthesis of GNRs, a key building block, that is 1,8-diaryl phenanthrene-2,7-diboronic acid pinacol ester **3** was synthesized in three steps with gram scale (Scheme S2),[9] which features with armchair and cove type edge (Scheme 1a). The introduction of sulfur to GNRs is achieved by the addition of 2,5-dibromothiophene **2** as the functional block. In addition, 2-substituted biphenyl **1** was introduced as the end block. Tert-butyl substituents were installed respectively on **1** and **3** to ensure the good solubility of the intermediates and the corresponding GNRs. With the key link block **3**, functional block **2**, and end block **1** in hand, a series of precursors of sulfur-doped **AR-*n*** were obtained and isolated through column chromatography in 53% (**4a**), 19% (**4b**), and 12% (**4c**) yield. By varying the end groups and adjusting the molar ratio of the three components, congeners with diverse lengths can be obtained (see Scheme S3 and Table S2 for further details).[10] The following ring-closing reactions of **4a** and **4b** by intramolecular oxidative cyclodehydrogenation in the presence of 2,3-dichloro-5,6-dicyano-1,4-benzoquinone (DDQ) and CF_3SO_3H gave the desired GNRs **AR-11** and **AR-17** in 95% and 93% yields, which were well-characterized by NMR analysis and HRMS. Due to the poor solubility of **AR-23**, well-resolved ^{1}H and ^{13}C NMR spectra could not be recorded. However, characterization was achieved by matrix-assisted laser desorption/ionization time-of-flight mass spectrometry (MALDI-TOF MS) (Scheme 1c and Figure S5). The Scholl reaction is conducted using superstoichiometric oxidants, limiting its scalability. To address these challenges, we also developed an electrochemical continuous flow Scholl reaction. This method eliminates the need for oxidants and enables the production of **AR-11** in larger quantities. The arc lengths and arc-shaped of **AR-11**, **AR-17** and **AR-23** are 2.10 nm, 37.2° for **AR-11**, 3.29 nm, 51.4° for **AR-17**, and 4.49 nm, 70.6° for **AR-23** based on density functional theory (DFT) optimized structures (Scheme 1a, Figure S7-S13). Source code of the program for the measurement of lengths and the arc-shaped was listed in Table S5. In addition, **AR-11** and **AR-17** were oxidized to give orange solid **ARO-11** and **ARO-17** with excessive *meta*-chloroperoxybenzoic acid (*m*CPBA) in 90% yields (Scheme 1b).

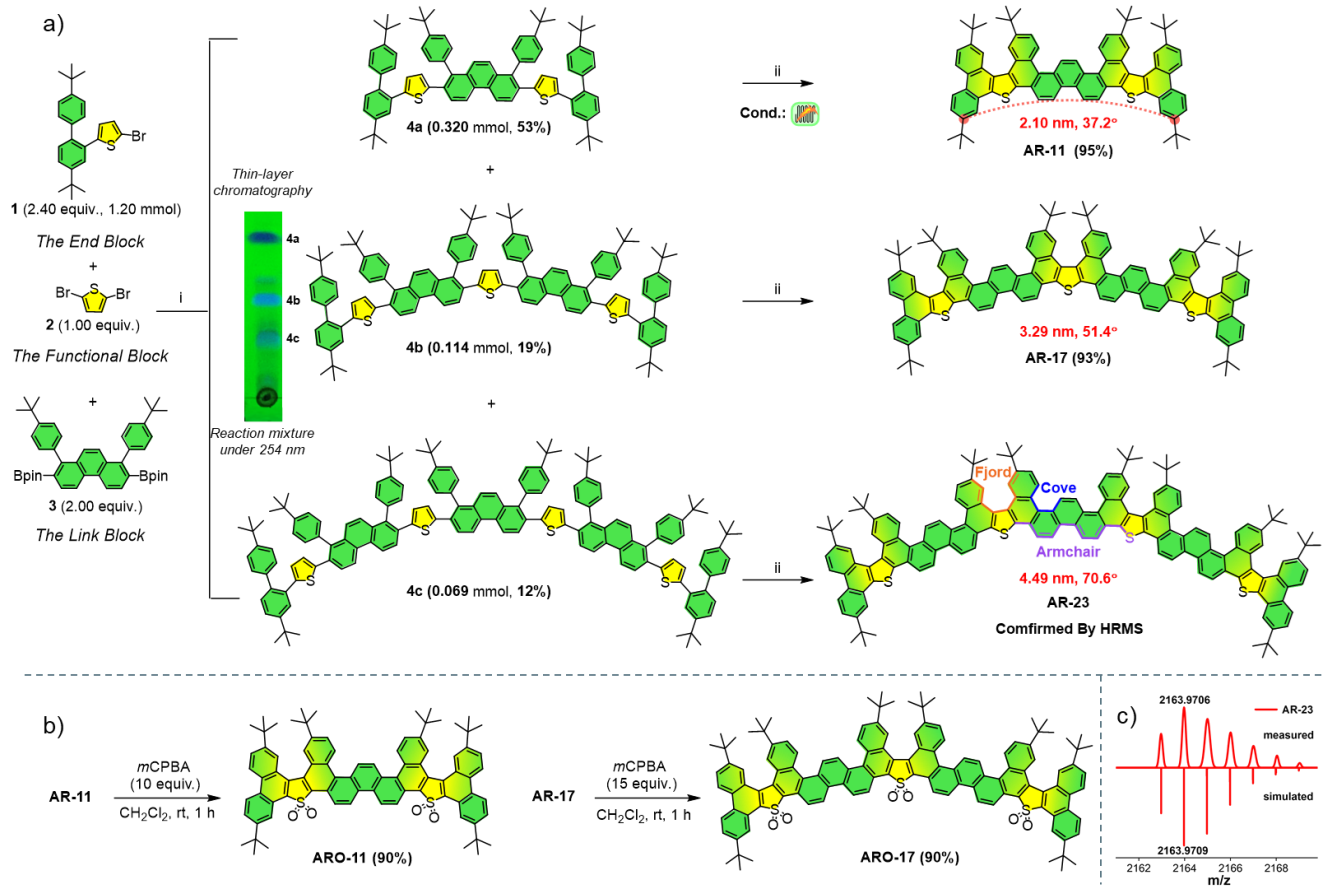

Scheme 1. a) (i) **1** (2.4 equiv.), **2** (1.0 equiv.), **3** (2.0 equiv.), $Pd(PPh_3)_4$ (0.5 equiv.), K_2CO_3 (25 equiv.), 1,4-Dioxane:H_2O = 8:1; 90°C, 36 h. Isolated yields were based on the amount of compound **1**. (ii) DDQ (1.2 equiv. for each C–C bond), CF_3SO_3H, CH_2Cl_2, −10°C, 1 h. DDQ: 2,3-dichloro-5,6-dicyano-1,4-benzoquinoe. Electrochemical continuous flow conditions: a carbon anode, a Ni cathode, $^nBu_4NBF_4$(0.13 M), DCM/TFA, **4a** (0.1 mmol), 1.65 V, 0.10 mL/min, rt. b) Synthetic Route of **ARO-11** and **ARO-17**. c) High-resolution MALDI-TOF mass spectra of **AR-23**.

X-ray Crystal Structures

The arcuate and curved shape structures of **AR-11** and **ARO-11** were confirmed by single-crystal X-ray diffraction analysis (Figure 2). Slow diffusion of acetone into a $CDCl_3/CS_2$ solution of **AR-11** at room temperature resulted in the formation of **AR-11** single crystals. The single crystals of **ARO-11** were obtained by the slow diffusion of CH_3OH into the $CHCl_3$ solution. Single-crystal structure analysis indicated that the π-skeletons of **AR-11** and **ARO-11** are highly twisted along their longitudinal axes (Figure 2a, 2b). With the presence of bulky tert-butyl groups on the fjord edges of **AR-11** and **ARO-11**, the benzenoid rings adopt an interlacing "up-down" conformation with dihedral angles ranging from 36° to 47° (also see Figure S2). The end-to-end arc lengths for π-backbone of **AR-11** and **ARO-11** are 2.05 nm and 2.06 nm, respectively, which correspond with the DFT optimized structures (Scheme 1a). In the packing structures of **AR-11** and **ARO-11** (Figure 2c and 2d), every two identical molecules (shown in green and blue) surround each other in the form of face to edge, forming a dimer. This dimer presents a slip-stacked packing mode along the plane of the a-axis and c-axis. In the stacking structures of **AR-11**, the dimer with intermolecular π–π interactions with an interlayer distance as short as 3.3 Å (Figure 2c and Figure S3). In the crystal structure of **ARO-11** are 3.0 Å distance of π–π interactions between the adjacent molecules. Besides, there are face-to-edge intermolecular C–H…O hydrogen bonding interactions (2.5 Å) and the arrangement is closer for **ARO-11** (Figure 2d and Figure S3).

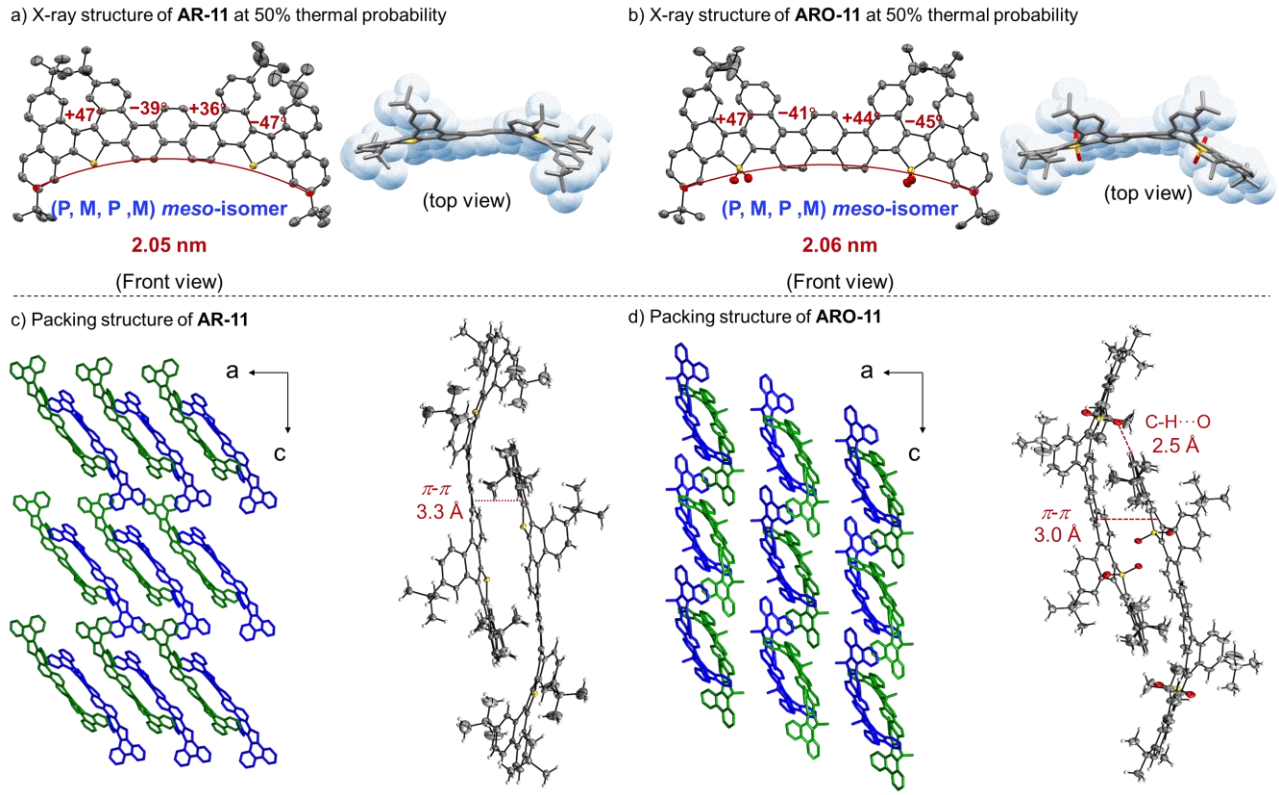

Figure 2. a, b): X-ray crystal structures of **AR-11** and **ARO-11**. (Thermal ellipsoids are shown at 50% probability.) c, d): The packing structure of **AR-11** and **ARO-11**. (Solvent molecules, hydrogen atoms and partial tertiary butyl are omitted for clarity).

Calculations and Photophysical Properties

Considering the 4-fold helicity of **AR-11**, we can depict ten stereoisomers including four pairs of enantiomers and two meso isomers (six diastereomers in total, Figure 3), which are categorized as follows: C_1 symmetry (C_1-I and C_1-II), C_2 symmetry (C_2-I and C_2-II), and C_s symmetry (C_s-I and C_s-II) (Figure 3). DFT calculations were performed to explore the relative stability of them. Calculation details are given in the Supporting Information (Figure S14-15).[11] Based on the DFT calculations, the (*P*,*M*,*P*,*M*) conformation is the most stable, which is consistent with the X-ray crystal structure result, followed by the alternated (*P*,*M*,*M*,*P*) (+0.9 kcal/mol). The conversion barrier of **AR-11** from the (*P*,*M*,*M*,*P*) to the (*P*,*M*,*P*,*M*) is 20.1 kcal/mol (Figure S15). Furthermore, **AR-17** exhibits 6-fold helicity and affords 36 types of isomers with varying Gibbs free energies (Figure S16). Semi-empirical calculations were conducted over them. Based on the calculations, (*P*,*M*,*P*,*M*,*P*,*M*,*P*) conformation is the most stable, followed by the alternated conformation (*P*,*M*,*P*,*M*,*P*,*P*,*M*) (+0.8 kcal/mol).

To gain insight into the length-dependent photophysical properties of **AR-*n*** and **ARO-*n***, UV/Vis absorption and fluorescence emission were measured in diluted CH_2Cl_2 solutions at room temperature (Figure 4a, 4b). The results are summarized in Table 1. **AR-17** (λ_{abs} = 434 nm, log ε = 5.24) exhibited a bathochromic shift compared to **AR-11** (λ_{abs} = 415 nm, log ε = 5.07), which was attributed to the extended π-backbone. **ARO-11** exhibited a pronounced bathochromic shift in its absorption maximum (λ_{abs} = 466 nm, log ε = 4.79) compared to **AR-11** as well, attributable to the integration of the electron-withdrawing thiophene-*S*,*S*-dioxide unit into the extended π-system. Notably, **ARO-11** displayed broader absorption features than **AR-11**. Similar trends were observed for **ARO-17** and **AR-17**.

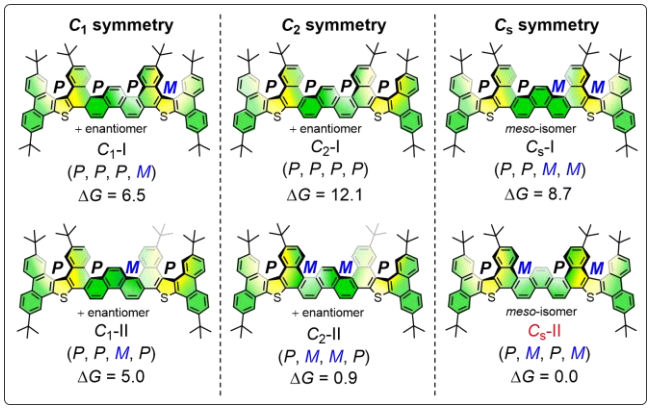

Figure 3. Stereoisomers of **AR-11** and their relative Gibbs free energies (kcal·mol^{-1}).

Compared to **AR-11** (λ_{em} = 459 nm), the bathochromic shift in the photoluminescence spectra was pronounced for **AR-17** (λ_{em} = 479 nm) due to its extended conjugated backbone, or for **ARO-11** (λ_{em} = 511 nm) due to incorporation of the electron-withdrawing thiophene-*S*,*S*-dioxide unit (Figure

4b). The absolute fluorescence quantum yields (Φ_F) were measured by using an integrating sphere detector.[12] In CH_2Cl_2 solution, Φ_F values increased with π-backbone extension in **AR-11** (15%) and **AR-17** (37%). Conversely, **ARO-11** (65%) and **ARO-17** (71%) displayed high, π-backbone-independent Φ_F values. In the solid state, however, Φ_F values decreased to 5.9% for **ARO-11** and 1.5% for **ARO-17**, likely due to aggregation-caused quenching via strong intermolecular π-overlap. Similar trends were observed for **AR-11** (4.7%) and **AR-17** (0.2%).[13] To further elucidate the photophysical properties, the energy diagrams and frontier molecular orbitals of **AR-n** and **ARO-n** were calculated by the time-dependent density functional theory (TD-DFT) method at the PBE0-D3(BJ)/6-31G(d,p) level of theory (Figure 4d and Figure S19-20).[14] The lowest energy absorption bands of **AR-n** and **ARO-n** are attributed to the S0→S1 excitation (ΔE, 3.12 eV for **AR-11**, 2.74 eV for **ARO-11**, 2.97 eV for **AR-17**, 2.61 eV for **ARO-17**), which mainly arises from the HOMO→LUMO transition (95% for **AR-11**, 92% for **ARO-11**, 90% for **AR-17**, 87% for **ARO-17**) and has an oscillator strength (f) of 1.77 for **AR-11**, 1.19 for **ARO-11**, 3.07 for **AR-17**, and 2.11 for **ARO-17** (Table S6-9). The electrochemical properties of these GNRs were studied in THF solution by cyclic voltammetry (CV) and differential pulse voltammetry (DPV). All compounds exhibited an obvious reduction process, with E_p^{red1} values of −1.51 eV (**AR-11**), −1.43 eV (**ARO-11**), −1.38 eV (**AR-17**), and −1.52 eV (**ARO-17**). Oxidation potentials (E_p^{ox1}) were 0.93 eV (**AR-11**), 1.03 eV (**ARO-11**), 1.01 eV (**AR-17**), and 1.00 eV (**ARO-17**). Based on E_p^{ox1} values, HOMO energy levels were estimated as −5.07 eV (**AR-11**), −5.14 eV (**ARO-11**), −5.12 eV (**AR-17**), and −5.08 eV (**ARO-17**), demonstrating good agreement with the computational study (Figure 4c, Scheme S5 and Table1).

Table 1 Spectroscopic Characterizations and Energy Levels of **AR-11, AR-17** and **ARO-11, ARO-17.**

compound	λ_{abs} [nm][a]	ε_{max} [10^5 M^{-1} cm^{-1}][a]	λ_{em} [nm][a]	Φ [%][a,c]	τ [ns][a,d]	Φ [%][b,c]	τ [ns][b,d]	E_{HOMO} [eV][e]	E_{HOMO} [eV][f]	E_{LUMO} [eV][f]	E_g [eV][f]
AR-11	415/392	1.19/1.01	459	15	2.07	4.7	0.67	−5.12	−5.06	−1.70	3.36
AR-17	434/410	1.74/1.56	479	37	4.02	0.2	0.54	−5.07	−5.03	−1.79	3.24
ARO-11	466/441	0.65/0.56	511	65	1.77	5.9	0.74	−5.14	−5.43	−2.40	3.03
ARO-17	486/463	1.04/0.92	530	71	1.77	1.5	1.24	−5.08	−5.40	−2.51	2.89

[a]Measured in CH_2Cl_2 solution (1.0×10^{-5} M).
[b]Measured in the solid state.
[c]Fluorescence quantum yield.
[d]Fluorescence lifetime.
[e]From CVs measured in THF (1.0×10^{-5} M). The HOMO energy levels are adjusted according to the redox half potential of Fc/Fc^+ and estimated. according to the formula E_{HOMO} (eV) = $-(4.80 + E_{onset}^{ox1} - E(_{Fc/Fc^+}))$ (also see Figure S3).
[f]Calculations were performed at the B3LYP/6-31G(d) level.

The energy levels of the calculated frontier molecular orbitals of **AR-*n*** and **ARO-*n*** are shown in Figure 4d and Figure S19-20, for example, the HOMO and LUMO of **AR-17** and **ARO-17** spread over the whole π-system. After converting the electron-rich thiophene ring into an electron-poor thiophene-*S*,*S*-dioxides, the sulfone dioxide unit considerably reduces the HOMO orbital energy level; the LUMO orbital energy level has a greater decrease. Hence, the energy gap of the molecule is greatly reduced, which leads to a large redshift of fluorescence emission. Notably, the band gaps of **AR-*n*** and **ARO-*n*** are well regulated from 3.90 eV of **AR-5** to 3.11 eV of **AR-23** and 3.43 eV of **ARO-5** to 2.81 eV of **ARO-23**. The energies of frontier orbitals of **AR-*n*** and **ARO-*n*** are plotted in Figure 4e (also see Figure S21-24). The decrement of the LUMO energy level and increment of the HOMO energy level are observed from **AR-5** to **AR-23**, which leads to a clear shrinkage of E_g in the same sequence. The decreased HOMO level for **ARO-*n*** compared with **AR-*n*** strongly suggests the enhanced affinity of **ARO-*n*** to electrons.

Notably, to illustrate the electronic structures and the molecular aromaticity of these GNRs, nucleus-independent chemical shifts (NICS) and anisotropy of the induced current densities (ACID) calculation on **AR-11** and **ARO-11** are conducted at the B3LYP/6-31G(d) level of theory based on the optimized structures (Figure 4f and Figure S17, 18).[15] The largely negative $NICS(1)_{ZZ}$ values (−22.9 to −27.6 of **AR-11**, −24.1 to −28.6 of **ARO-11** in yellow) indicate that these six-membered rings exhibit local aromaticity. These analyses are further supported by ACID calculations, which show clockwise (diamagnetic) ring currents mainly distributed at hexagonal rings A/B/C/D/E/F at the outer rims of the whole *π*-framework. In addition, rings J/L in **AR-11** and **ARO-11** also display very negative $NICS(1)_{ZZ}$ values(−20.3 of **AR-11**, −20.6 of **ARO-11**), manifesting that they also contribute to the aromatic structures. However, the positive $NICS(1)_{ZZ}$ values of 13.3 suggest that these sulfur dioxide rings have no contribution to the overall *π*-conjugation in Figure 4f. The induced ring currents are relatively weak in the fused sulfur dioxide rings H/N of **ARO-11**, resulting in breaks for the global delocalization of the *π*-electrons (Figure 4f). These results demonstrate that the doping of sulfur dioxide achieves the delocalization of *π*-electrons in GNRs.

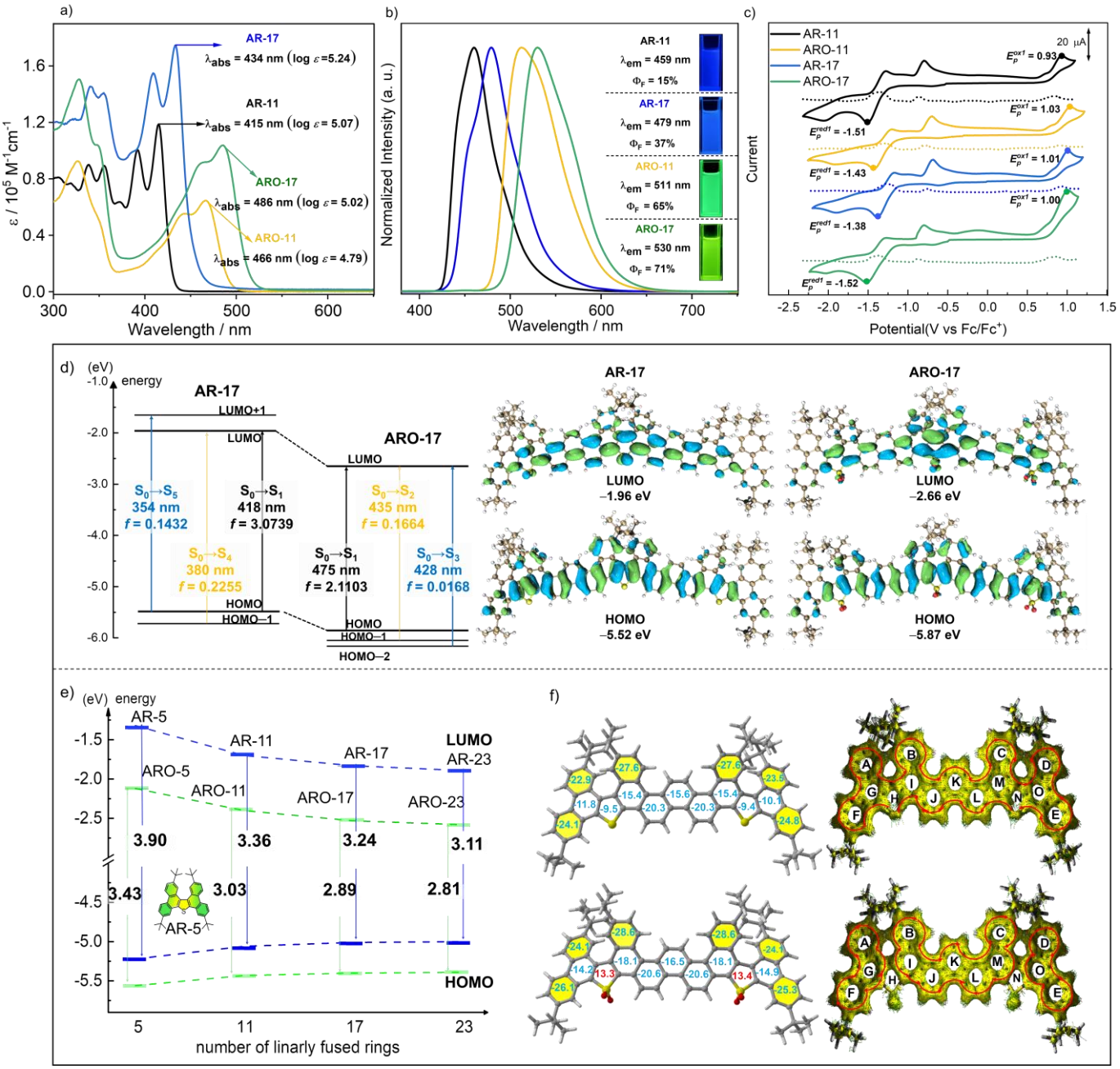

Figure 4. a): UV/Vis absorption spectra (**AR-11**: black line; **AR-17**: blue line; **ARO-11**: orange line; **ARO-17**: green line) in CH_2Cl_2 solution. b): Photoluminescence spectrum in CH_2Cl_2 solution (λ_{ex} = 300 nm). c): CV and DPV of **AR-11**, **ARO-11** and **AR-17**, **ARO-17** in THF solution containing 0.1 M Bu_4NPF_6 at room temperature at a scan rate of 0.1 V/s. (1.0×10^{-5} mol/L in THF for CV and DPV). d): Energy diagrams and frontier molecular orbitals of **AR-17** and **ARO-17** calculated at the PBE0-D3(BJ)/6-31G(d,p) level of theory (unit: eV). e): HOMO and LUMO energies of **AR-*n*** (blue dotted line), and **ARO-*n*** (green dotted line), calculated at the B3LYP/6-31G(d) level of theory. f): Calculated NICS(1)$_{ZZ}$ values and ACID plots (contribution from π electrons only) of **AR-11** and **ARO-11** at the B3LYP/6-31G(d) level of theory. Aromatic sextet rings are shown in yellow.

Conclusions

Graphene nanoribbons (GNRs) hold significant promise for optoelectronic applications, but their development is hampered by the limitations of traditional iterative synthetic methods. These methods often involve complex and expensive starting materials, restricting structural and functional diversity. This hinders the rapid exploration of structure-property relationships, especially length-dependent properties of GNRs, and the discovery of high-performance materials. A more efficient approach is to employ a modular "shotgun" synthesis, using end blocks, link blocks, and functional blocks as key components. This strategy allows for the facile synthesis of GNRs with a wide range of structures and functionalities by simply varying the functional block. we have demonstrated a highly efficient "shotgun" synthetic approach for sulfur-doped GNRs featuring a unique cove-armchair-fjord edge combination. Notably, sulfur incorporation into the backbone yielded arc-shaped GNRs. The unambiguous crystallographic characterization of **AR-11** and **ARO-11** reveals that the combined cove and fjord edge structure causes it to deviate from planarity due to steric repulsion. By oxidizing the electron-rich sulfur atoms to electron-deficient sulfones, we effectively tune the electronic properties of GNRs. Expanding the GNR family further, we're currently exploring the versatility of shotgun synthesis by crafting GNRs adorned with diverse heteroatom dopants.

EXPERIMENTAL PROCEDURES

Resource availability

Lead contact

Further information and requests for resources should be directed to and will be fulfilled by the lead contact, Yuanming Li (yuanming.li@fzu.edu.cn).

Materials availability

Subject to availability, all stable reagents generated in this study will be made available on request, but we might require a payment and/or a completed materials transfer agreement if there is potential for commercial application.

Data and code availability

The Cartesian coordinates for the molecular models reported in this article are included in Data S9. The crystallographic data for **AR-11** and **ARO-11** reported in this article have been deposited at the Cambridge Crystallographic Data Centre (CCDC) under deposition numbers CCDC:2303699–2303698, respectively. These data can be obtained free of charge from theCCDC at http://www.ccdc. cam.ac.uk/data_request/cif. Other data supporting this study are available in the article and supplemental information.

SUPPLEMENTAL INFORMATION

Supplemental information can be found online.

ACKNOWLEDGMENTS

We thank Prof. Weiguo Huang (Fujian Institute of Research on the Structure of Matter, Chinese Academy of Sciences) for the single crystal measurement, Prof. Kenichiro Itami (Nagoya University), Prof. Akiko Yagi (Nagoya University), Prof. Chenguang Wang (Jilin University) and Prof. Chaolumen (Inner Mongolia University) for constructive criticism of the manuscript.

AUTHOR CONTRIBUTIONS

Y.L. conceived and directed the project. K.Y. directed the electrochemical synthesis section R.Z. conducted most of the experiments. X.C. performed the DFT calculations. L.Z. and Y.H. and Z.Z. contributed to the synthesis, Q.W. and L.W. and T.W. analyzed the data. W.W. conducted the electrochemical synthesis. All authors discussed the results and commented on the manuscript.

DECLARATION OF INTERESTS

The authors declare no competing interests.

REFERENCES

(1) (a) Wu, J.; Pisula, W.; Müllen, K. Graphenes as Potential Material for Electronics. *Chem. Rev.* **2007**, *107*, 718-747. (b) Li, X.; Wang, X.; Zhang, L.; Lee, S.; Dai, H. Chemically Derived, Ultrasmooth Graphene Nanoribbon Semiconductors. *Science* **2008**, *319*, 1229-1232. (c) Segawa, Y.; Ito, H.; Itami, K. Structurally uniform and atomically precise carbon nanostructures. *Nat. Rev. Mater.* **2016**, *1*, 15002. (d) Yoon, K.-Y.; Dong, G. Liquid-phase bottom-up synthesis of graphene nanoribbons. *Mater. Chem. Front.* **2020**, *4*, 29-45. (e) Yano, Y.; Mitoma, N.; Ito, H.; Itami, K. A Quest for Structurally Uniform Graphene Nanoribbons: Synthesis, Properties, and Applications. *J. Org. Chem.* **2020**, *85*, 4-33. (f) Houtsma, R. S. K.; de la Rie, J.; Stöhr, M. Atomically precise graphene nanoribbons: interplay of structural and electronic properties. *Chem. Soc. Rev.* **2021**, *50*, 6541-6568. (g) Gu, Y.; Qiu, Z.; Müllen, K. Nanographenes and Graphene Nanoribbons as Multitalents of Present and Future Materials Science. *J. Am. Chem. Soc.* **2022**, *144*, 11499-11524. (h) Wang, M.-W.; Fan, W.; Li, X.; Liu, Y.; Li, Z.; Jiang, W.; Wu, J.; Wang, Z. Molecular Carbons: How Far Can We Go? *ACS. Nano.* **2023**, *17*, 20734-20752.

(2) (a) Yazyev, O. V. A Guide to the Design of Electronic Properties of Graphene Nanoribbons. *Acc. Chem. Res.* **2013**, *46*, 2319-2328. (b) Liu, J.; Li, B.-W.; Tan, Y.-Z.; Giannakopoulos, A.; Sanchez-Sanchez, C.; Beljonne, D.; Ruffieux, P.; Fasel, R.; Feng, X.; Müllen, K. Toward Cove-Edged Low Band Gap Graphene Nanoribbons. *J. Am. Chem. Soc.* **2015**, *137*, 6097-6103. (c) Yao, X.; Zheng, W.; Osella, S.; Qiu, Z.; Fu, S.; Schollmeyer, D.; Müller, B.; Beljonne, D.; Bonn, M.; Wang, H. I.; Müllen, K.; Narita, A. Synthesis of Nonplanar Graphene Nanoribbon with Fjord Edges. *J. Am. Chem. Soc.* **2021**, *143*, 5654-5658. (d) Wang, Y.; Huang, Y.; Huang, T.; Zhang, J.; Luo, T.; Ni, Y.; Li, B.; Xie, S.; Zeng, Z. Perylene-Based Linear Nonalternant Nanoribbons with Bright Emission and Ambipolar Redox Behavior. *Angew. Chem., Int. Ed.* **2022**, *61*, e202200855. (e) Liu, K.; Zheng, W.; Osella, S.; Qiu, Z.-L.; Böckmann, S.; Niu, W.; Meingast, L.; Komber, H.; Obermann, S.; Gillen, R.; Bonn, M.; Hansen, M. R.; Maultzsch, J.; Wang, H. I.; Ma, J.; Feng, X. Cove-Edged Chiral Graphene

Nanoribbons with Chirality-Dependent Bandgap and Carrier Mobility. *J. Am. Chem. Soc.* **2024**, *146*, 1026-1034.
(3) (a) Kawai, S.; Nakatsuka, S.; Hatakeyama, T.; Pawlak, R.; Meier, T.; Tracey, J.; Meyer, E.; Foster, A. S. Multiple heteroatom substitution to graphene nanoribbon. *Sci. Adv.* **2018**, *4*, eaar7181. (b) Wang, X.-Y.; Yao, X.; Narita, A.; Müllen, K. Heteroatom-Doped Nanographenes with Structural Precision. *Acc. Chem. Res.* **2019**, *52*, 2491-2505. (c) Borissov, A.; Maurya, Y. K.; Moshniaha, L.; Wong, W.-S.; Żyła-Karwowska, M.; Stępień, M. Recent Advances in Heterocyclic Nanographenes and Other Polycyclic Heteroaromatic Compounds. *Chem. Rev.* **2022**, *122*, 565-788. (d) Sano, Y.; Shintani, T.; Hayakawa, M.; Oda, S.; Kondo, M.; Matsushita, T.; Hatakeyama, T. One-Shot Construction of BN-Embedded Heptadecacene Framework Exhibiting Ultra-narrowband Green Thermally Activated Delayed Fluorescence. *J. Am. Chem. Soc.* **2023**, *145*, 11504-11511.
(4) (a) Chen, L.; Hernandez, Y.; Feng, X.; Müllen, K. From Nanographene and Graphene Nanoribbons to Graphene Sheets: Chemical Synthesis. *Angew. Chem., Int. Ed.* **2012**, *51*, 7640-7654. (b) Liu, J.; Feng, X. Synthetic Tailoring of Graphene Nanostructures with Zigzag-Edged Topologies: Progress and Perspectives. *Angew. Chem., Int. Ed.* **2020**, *59*, 23386-23401. (c) Chen, W.; Yu, F.; Xu, Q.; Zhou, G.; Zhang, Q. Recent Progress in High Linearly Fused Polycyclic Conjugated Hydrocarbons (PCHs, n > 6) with Well-Defined Structures. *Adv. Sci.* **2020**, *7*, 1903766. (d) Jolly, A.; Miao, D.; Daigle, M.; Morin, J.-F. Emerging Bottom-Up Strategies for the Synthesis of Graphene Nanoribbons and Related Structures. *Angew. Chem., Int. Ed.* **2020**, *59*, 4624-4633.
(5) (a) Grzybowski, M.; Skonieczny, K.; Butenschön, H.; Gryko, D. T. Comparison of Oxidative Aromatic Coupling and the Scholl Reaction. *Angew. Chem., Int. Ed.* **2013**, *52*, 9900-9930. (b) Zhang, Y.; Pun, S. H.; Miao, Q. The Scholl Reaction as a Powerful Tool for Synthesis of Curved Polycyclic Aromatics. *Chem. Rev.* **2022**, *122*, 14554-14593. (c) Zhong, Y.; Kumar, B.; Oh, S.; Trinh, M. T.; Wu, Y.; Elbert, K.; Li, P.; Zhu, X.; Xiao, S.; Ng, F.; Steigerwald, M. L.; Nuckolls, C. Helical Ribbons for Molecular Electronics. *J. Am. Chem. Soc.* **2014**, *136*, 8122-8130. (d) Daigle, M.; Picard-Lafond, A.; Soligo, E.; Morin, J.-F. Regioselective Synthesis of Nanographenes by Photochemical Cyclodehydrochlorination. *Angew. Chem., Int. Ed.* **2016**, *55*, 2042-2047. (e) Kato, K.; Segawa, Y.; Scott, L. T.; Itami, K. A Quintuple [6]Helicene with a Corannulene Core as a C5-Symmetric Propeller-Shaped π-System. *Angew. Chem., Int. Ed.* **2018**, *57*, 1337-1341. (f) Hagui, W.; Doucet, H.; Soulé, J.-F. Application of Palladium-Catalyzed C(sp2)–H Bond Arylation to the Synthesis of Polycyclic (Hetero)Aromatics. *Chem* **2019**, *5*, 2006-2078. (g) Yang, W.; Lucotti, A.; Tommasini, M.; Chalifoux, W. A. Bottom-Up Synthesis of Soluble and Narrow Graphene Nanoribbons Using Alkyne Benzannulations. *J. Am. Chem. Soc.* **2016**, *138*, 9137-9144. (h) Li, Y. L.; Zee, C.-T.; Lin, J. B.; Basile, V. M.; Muni, M.; Flores, M. D.; Munárriz, J.; Kaner, R. B.; Alexandrova, A. N.; Houk, K. N.; Tolbert, S. H.; Rubin, Y. Fjord-Edge Graphene Nanoribbons with Site-Specific Nitrogen Substitution. *J. Am. Chem. Soc.* **2020**, *142*, 18093-18102. (i) Narita, A.; Chen, Z.; Chen, Q.; Müllen, K. Solution and on-surface synthesis of structurally defined graphene nanoribbons as a new family of semiconductors. *Chem. Sci.* **2019**, *10*, 964-975.
(6) (a) Yang, X.; Elbert, S. M.; Rominger, F.; Mastalerz, M. A Series of Soluble Thieno-Fused Coronene Nanoribbons of Precise Lengths. *J. Am. Chem. Soc.* **2022**, *144*, 9883-9892. (b) Boddeda, A.; Hossain, M. M.; Saeed Mirzaei, M.; Lindeman, S. V.; Mirzaei, S.; Rathore, R. Angular ladder-type meta-phenylenes: synthesis and electronic structural analysis. *Org. Chem. Front.* **2020**, *7*, 3215-3222.
(7) Jasti, R.; Bhattacharjee, J.; Neaton, J. B.; Bertozzi, C. R. Synthesis, Characterization, and Theory of [9]-, [12]-, and [18]Cycloparaphenylene: Carbon Nanohoop Structures. *J. Am. Chem. Soc.* **2008**, *130*, 17646-17647.
(8) (a) Segawa, Y.; Miyamoto, S.; Omachi, H.; Matsuura, S.; Šenel, P.; Sasamori, T.; Tokitoh, N.; Itami, K. Concise Synthesis and Crystal Structure of [12]Cycloparaphenylene. *Angew. Chem., Int. Ed.* **2011**, *50*, 3244-3248. (b) Zhu, L.; Xu, J.; Lan, B.; Chen, X.; Kono, H.; Xu, H.; Yan, J.; Li, W.; Yagi, A.; Yuan, Y.; Itami, K.; Li, Y. Ferrocene-based conjugated macrocycles: shotgun synthesis, size-dependent properties and tunable fluorescence intensity. *Org. Chem. Front.* **2024**, *11*, 5130-5137. (c) Xu, J.; Lan, B.; Zhu, L.; Xu, H.; Chen, X.; Li, W.; Yuan, Y.; Yan, J.; Li, Y. Synthesis and Properties of Ferrocene Conjugated Macrocycles with Illusory Topology of the Penrose Stairs. *Chem. Res. Chin. U.* **2024**, *40*, 881-886. (d) Lan, B.; Xu, J.; Zhu, L.; Chen, X.; Kono, H.; Wang, P.; Zuo, X.; Yan, J.; Yagi, A.; Zheng, Y.; Chen, S.; Yuan, Y.; Itami, K.; Li, Y. Side-Chain Type Ferrocene Macrocycles. *Precision Chemistry* **2024**, *2*, 143-150.
(9) Li, Y.; Yagi, A.; Itami, K. Synthesis of sterically hindered 4,5-diarylphenanthrenes via acid-catalyzed bisannulation of benzenediacetaldehydes with alkynes. *Chem. Sci.* **2019**, *10*, 5470-5475.
(10) When 2-bromo-4,4'-di-tert-butyl-1,1'-biphenyl was employed as the end-capping compound, the yields of **4a** and **4b** decreased to 30% and 16%, respectively (Scheme S3).
(11) (a) See the Supporting Information for full citation of Gaussian 16. (b) Neese, F. Software update: The ORCA program system—Version 5.0. *WIREs Comput Mol Sci* **2022**, *12*, e1606. (c) Neese, F. Software update: the ORCA program system, version 4.0. *WIREs Comput Mol Sci* **2018**, *8*, e1327. (d) Mardirossian, N.; Head-Gordon, M. ωB97M-V: A combinatorially optimized, range-separated hybrid, meta-GGA density functional with VV10 nonlocal correlation. *J. Chem. Phys.* **2016**, *144*. (e) Chai, J.-D.; Head-Gordon, M. Long-range corrected hybrid density functionals with damped atom–atom dispersion corrections. *Phys. Chem. Chem. Phys.* **2008**, *10*, 6615-6620. (f) Weigend, F. Accurate Coulomb-fitting basis sets for H to Rn. *Phys. Chem. Chem. Phys.* **2006**, *8*, 1057-1065. (g) Weigend, F.; Ahlrichs, R. Balanced basis sets of split valence, triple zeta valence and quadruple zeta valence quality for H to Rn: Design and assessment of accuracy. *Phys. Chem. Chem. Phys.* **2005**, *7*, 3297-3305.
(12) Würth, C.; Grabolle, M.; Pauli, J.; Spieles, M.; Resch-Genger, U. Relative and absolute determination of fluorescence quantum yields of transparent samples. *Nature Protocols.* **2013**, *8*, 1535-1550.
(13) (a) Dexter, D. L.; Schulman, J. H. Theory of Concentration Quenching in Inorganic Phosphors. *J. Chem. Phys.* **1954**, *22*, 1063-1070. (b) Kasha, M.; Rawls, H.; El-Bayoumi, M. The exciton model in molecular spectroscopy, Pure Appl. Chem.11, 371-392. *Pure Appl. Chem.,* **1965**, *11*, 371-392. (c) Chen, R. F.; Knutson, J. R. Mechanism of fluorescence concentration quenching of carboxyfluorescein in liposomes: energy transfer to nonfluorescent dimers. *Anal. Biochem.* **1988**, *172*, 61-77.
(14) Lu, T.; Chen, F. Multiwfn: A multifunctional wavefunction analyzer. *J. Comput. Chem.* **2012**, *33*, 580-592.
(15) Randić, M. Aromaticity of Polycyclic Conjugated Hydrocarbons. *Chem. Rev.* **2003**, *103*, 3449-3606.